International Journal of Coal Geology 123 (2014) 62–68

Contents lists available at ScienceDirect

International Journal of Coal Geology

journal homepage: www.elsevier.com/locate/ijcoalgeo

Klinkenberg effect on predicting and measuring helium permeability in gas shales

Mahnaz Firouzi, Khalid Alnoaimi, Anthony Kovscek, Jennifer Wilcox *

Department of Energy Resources Engineering, Stanford University, Stanford, CA 94305-2220, USA

ARTICLE INFO

Article history:
Received 21 June 2013
Received in revised form 24 September 2013
Accepted 24 September 2013
Available online 1 October 2013

Keywords:
Klinkenberg
Molecular modeling
Measurement
Helium
Permeability
Shale

ABSTRACT

To predict accurately gas-transport in shale systems, it is important to study the transport phenomena of a non-adsorptive gas such as helium to investigate gas "slippage". Non-equilibrium molecular dynamics (NEMD) simulations have been carried out with an external driving force imposed on the 3-D carbon pore network generated atomistically using the Voronoi tessellation method, representative of the carbon-based kerogen porous structure of shale, to investigate helium transport and predict Klinkenberg parameters. Simulations are conducted to determine the effect of pressure on gas permeability in the pore network structure. In addition, pressure pulse decay experiments have been conducted to measure the helium permeability and Klinkenberg parameters of a shale core plug to establish a comparison between permeability measurements in the laboratory and the permeability predictions using NEMD simulations. The results indicate that the gas permeability, obtained from pulse-decay experiments, is approximately two orders of magnitude greater than that calculated by the MD simulation. The experimental permeability, however, is extracted from early-time pressure profiles that correspond to convective flow in shale macropores (>50 nm). That is, pore diameters estimated from the measured permeability are greater than 50 nm.

1. Introduction

Although theories of gas transport in porous media have been used and applied in the past, specific complexities such as material and pore-size heterogeneities make each case unique. Gas transport through tight sands, unmineable coal seams, and unconventional shale gas reservoirs are some examples in which more reliable and precise modeling is required (Chawathe et al., 1996; Ertekin et al., 1986; Jalali and Mohaghegh, 2004). Coal and the organic components of gas shale are comprised of extremely complex pore networks with varying pore size, shape, and surface functionality, that are partially responsible for uncertainties in permeability and flux estimates based upon Navier–Stokes approaches. It is important to understand the gas' interaction with its local surroundings on the molecular-scale to predict accurately the permeability and gas behavior in the confined pores of these natural systems. SEM (scanning electron microscopy) images of shale samples showed pore widths in the macro (>50 nm) and meso (2 nm < meso < 50 nm) scales within the shale fabric (Sondergeld et al., 2010) while STEM (scanning tunneling electron microscopy) images can capture pore widths in shales down to 2 nm (Curtis et al., 2011). A conventional SEM technique can image an area between 1 cm to 5 μm with a spatial resolution of 50 nm 100 nm and a magnification from 20× to 30,000× (Vijaya et al., 2012). Gas transport in shale cores may exhibit a combination of Darcy and slip flow due to multiple pore widths (Javadpour and Fisher, 2007). One way to characterize the gas transport regimes in a shale core is by studying the Knudsen number. The Knudsen number is a dimensionless parameter that relates the gas mean free path to the average pore size of the sample as:

$$K_n = \frac{\lambda}{d} \tag{1}$$

where K_n is the Knudsen number, λ is the gas mean free path and d is the average pore diameter. The mean free path of the gas is defined as (Mulder, 1991):

$$\lambda = \frac{k_B T}{\pi d^2 P \sqrt{2}}, \tag{2}$$

where k_B is the Boltzmann constant, T is temperature and P is pressure. Table 1 shows Knudsen numbers that correspond to different flow regimes (Hadjiconstantinou, 2006).

If for example, the average pore diameter is 100 nm and the mean free path at a given pressure is 5 nm, the Knudsen number would be approximately 0.05 thereby indicating a slip transport regime. Clearly, a variety of flow types might occur in a porous medium with a range of pore sizes from nm to hundreds of nm.

The classical Navier–Stokes hydrodynamics is known to describe the macroscopic flow of simple fluids (Travis et al., 1997). Gas transport in pores on the order of microns (i.e., 10^{-6} m) such as sandstones of depleted oil and gas reservoirs is governed by Darcy's law derived from the Navier–Stokes equation by using a formal averaging procedure (Neuman, 1977; Whitaker, 1986). Here, the continuum flow assumption

* Corresponding author.
E-mail address: jen.wilcox@stanford.edu (J. Wilcox).

0166-5162/$ – see front matter © 2013 Elsevier B.V. All rights reserved.
http://dx.doi.org/10.1016/j.coal.2013.09.006

Table 1
Knudsen number and flow types.

Flow type	Knudsen number
Continuum flow	$K_n < 10^{-3}$
Slip flow	$10^{-3} < K_n < 10^{-1}$
Transition flow	$10^{-1} < K_n < 10^{1}$
Free-molecule flow	$10^{1} < K_n$

is valid. Flow through very narrow channels or pores may not be accurately described based upon these traditional macroscopic approaches (Travis et al., 1997). When temperature and density vary appreciably on a scale comparable to the molecular mean free path, these equations break down (Bitsanis et al., 1988). Therefore, as pores become smaller, the flow no longer obeys Darcy's law and correction factors associated with the transport may be required (Ertekin et al., 1986; Jones and Owens, 1980). In micro- and mesopores unlike in macropores (where continuum flow occurs), the gas velocity at the walls is *non-zero*, and predicted gas transport is enhanced as the "gas slippage" reduces viscous drag and increases the apparent permeability (Klinkenberg, 1941). Gas molecules are transported along the walls by molecular streaming or Knudsen diffusion due to gas slippage and surface hopping of adsorbed gas molecules (Akkutlu and Fathi, 2012). The slippage effect in carbon micropores and its influence on CO_2 and CH_4 transport were investigated in detail in the previous work by the authors (Firouzi and Wilcox, 2013).

Klinkenberg observed that in the pore capillary system the mean free path (λ) is inversely proportional to the mean pressure (p_m) and combined Poiseuille's Law for gas flow in capillaries with Darcy's law for flow in porous media, to obtain the Klinkenberg equation:

$$k_g = k_\infty \left(1 + \frac{b}{p_m}\right), \tag{3}$$

where k_∞ is the permeability at infinite pressure (liquid permeability) and b is referred to as the gas slippage factor (Klinkenberg, 1941; McPhee and Arthur, 1991). The mean free path is inversely proportional to the mean pressure, therefore, at lower pressures, the mean free path increases, and the slippage effect and subsequent gas permeability are enhanced. At larger mean pressures, the slippage effect is suppressed and permeability is reduced until at infinite mean pressure the mean free path is reduced to zero at which point the gas molecules are considered to behave as a liquid, with the gas and inert liquid permeability, k_∞, becoming equivalent (McPhee and Arthur, 1991). Under the assumptions of Klinkenberg, a thin layer exists close to the pore wall in which only collisions between the gas and wall take place, with gas–gas interactions ignored (Bravo, 2007).

Fundamental understanding of the microstructure of coal and gas shale and their influence on gas transport is of great importance in carbon capture and storage and recovery of natural gas (Gamson et al., 1993). To understand the molecular processes, gas transport phenomena in the matrix require further investigation. The gas transport is dominated by the geometrical and topological characteristics of the material as shown in the previous studies (Firouzi and Wilcox, 2012; Firouzi et al., 2004; Sahimi and Tsotsis, 2003; Xu et al., 2000a). The use of a single carbon slit pore is a grossly inadequate model to predict gas permeability in real porous natural systems. In order to predict the gas permeability using a more realistic model, a 3-D carbon-pore network structure is used in this work as generated atomistically using the Voronoi tessellation method. Recently a new method has been developed that generates the pore space based upon mimicking the chemical process that leads to its formation (Naserifar et al., 2013a,b).

To provide a baseline comparison, it is important to study the properties of a nonadsorbing gas, such as helium, to investigate the slippage phenomenon independent of adsorption. In addition, small molecules such as helium and hydrogen are able to permeate most pores. Therefore, to reveal the complex structure of coal and shale the gas permeation characteristics of small molecules are important to develop a fundamental understanding of the phenomena involved during the gas transport in these geologic formations. In the current work we investigate helium transport in the generated 3-D carbon pore network to predict the permeability and Klinkenberg parameters. NEMD simulations are used. This technique is ideally suited for the experimental situation in which an external driving force, such as a chemical potential or pressure gradient, is applied to a given pore or pore network. A dual control-volume-grand-canonical molecular dynamics (DCV-GCMD) technique, that has been used extensively (Cracknell et al., 1995; Firouzi et al., 2003, 2004, 2006, 2007; Ford and Glandt, 1995; Ford and Heffelfinger, 1998; Furukawa et al., 1997; Heffelfinger and Ford, 1998; Heffelfinger and Swol, 1994; Kjelstrup and Hafskjold, 1996; Lupkowski and Swol, 1991; MacElroy, 1994; Maginn et al., 1993; Nicholson et al., 1996; Pohl and Heffelfinger, 1999; Sun and Ebner, 1992; Sunderrajan et al., 1996; Thompson et al., 1998; Xu et al., 1998, 1999, 2000a,b) has been utilized. MD simulation studies were used in the past to study the effect of membrane structures and dynamics on gas permeation properties through microporous amorphous silica membranes, where helium was adopted as a permeating gas species (Yoshioka et al., 2008).

In addition, pulse-decay experiments are conducted to compare the permeability results of helium with those obtained by MD simulations. This comparison begins to address the current gap between the experimental analysis of shale gas permeability at core scale and theoretical analysis at pore scale. The pressure pulse decay method leads to more rapid determination of the permeability of tight media in comparison to a steady-state experiment that requires the flow rate to stabilize. To obtain permeability, the pressure pulse decay experiment has been simulated numerically and the downstream and upstream pressure histories have been matched simultaneously using a continuum description of the gas phase (Alnoaimi and Kovscek, 2013). Unlike many other solutions for permeability measurements (Amaefule et al., 1986; Brace et al., 1968; Dicker and Smits, 1988), our numerical history-match method provides a sufficiently accurate permeability determination for large pressure pulses. Elsewhere (Alnoaimi and Kovscek, 2013), the method has been described extensively and has been compared with the analytical solutions of Brace et al. (1968) and Jones (1997) for various gases including helium.

To date little fundamental knowledge exists regarding gas transport and slippage in the confined spaces of the natural system such as coal and shale for comparing theory and experiments. This work represents the steps required for a deeper understanding of the phenomena involved during the gas transport in these systems to address the gap between experimental analysis of gas permeability at core scale and theoretical analysis at pore scale.

2. Computational methodology

2.1. Carbon porous structure

A pore network model with a realistic 3-D carbon-based porous structure is used to predict the gas permeabilities. The pore network is generated by the Voronoi tessellation of a solid material composed of hundreds of thousands of atoms, and by designating a fraction of the Voronoi polyhedra as the pores that allows for the investigation of the effect of the morphology of the pore space, i.e., its pore size distribution and pore connectivity, on the gas transport (Firouzi and Wilcox, 2012, 2013). In this method a 3-D cell of carbon atoms with a structure corresponding to graphite is generated so that the number density of carbon atoms is 114 nm^{-3} and the spacing between the adjacent graphite layers in the z direction is 0.335 nm. The size of the initial graphite cell is 102, 103, and 103 Å in x, y, and z directions, respectively, and consists of 124,992 carbon atoms. Periodic boundary conditions are applied in all directions. The graphite cell is then tessellated, using the procedures

described in detail in the previous works (Firouzi and Wilcox, 2012, 2013). In this work the structure is rigid and the porosity in the generated 3-D pore network is 25% and the pores are selected randomly, with an average pore size of 20 Å. The number of inserted Poisson points in the simulation cell is 240. Although the porosity used for MD simulations may appear to be large, Vega et al. (submitted for publication) have imaged the spatial distribution of porosity in core-sized samples of the Eagle Ford shale. They find localized volumes of shale with porosities similar to 25% in core that has an average porosity of 5.4%.

2.2. Molecular modeling and interaction potential

The DCV-GCMD method is employed to investigate gas transport. This method combines the MD moves in the entire system with grand-canonical Monte Carlo (GCMC) insertions and deletions of the molecules in the two control volumes (CVs). The densities, or the corresponding chemical potentials, in the CVs are maintained using a sufficient number of GCMC insertions and deletions (Cracknell et al., 1995; Firouzi and Wilcox, 2012; Firouzi et al., 2003, 2004, 2006, 2007; Ford and Heffelfinger, 1998; Heffelfinger and Swol, 1994; Xu et al., 1998, 1999, 2000a,b). The probability of inserting a molecule is given by:

$$p^{+} = min\left\{\frac{ZV_c}{N+1} exp(-\Delta U/k_B T), 1\right\}, \tag{4}$$

where $Z = \exp(\mu / k_B T) / \Lambda^3$ is the absolute activity at temperature T, Λ and μ are, respectively, the de Broglie wavelength (Λ) and the chemical potential, k_B is the Boltzmann's constant, ΔU is the potential energy change resulting from inserting or removing a molecule, and V_c and N are the volume of the CV and number of molecules in each CV, respectively. The probability of deleting a molecule is given by:

$$p^{-} = \min\left\{\frac{N}{ZV_c} exp(-\Delta U/k_B T), 1\right\}. \tag{5}$$

The chemical potentials are converted to equivalent pressures using the Lennard-Jones (LJ) equation of state (Johnson et al., 1993). A thermal velocity selected from the Maxwell–Boltzmann distribution at the given T is assigned when a molecule is inserted in a CV. Typically, 10 GCMC insertions and deletions in each CV are followed by one MD integration step. In the MD simulations the Verlet velocity algorithm was used to integrate the equations of motion with a time step, $\Delta t = 0.00685$ ps. The equations of motion were integrated with up to 10×10^6 time steps to ensure that a steady state has been reached. The properties, such as concentration profiles, fluxes, etc., are calculated and averaged over the last 1 million time steps. The DCV-GCMD method has been explained in detail in the previous work by the authors (Firouzi and Wilcox, 2012, 2013; Firouzi et al., 2003, 2004, 2006, 2007).

The helium molecules were represented using LJ potentials and characterized by the effective LJ size and energy parameters, σ and ε, respectively. We used $\sigma_{He} = 2.64$ Å, and $\varepsilon_{He}/k_B = 10.9$ K. The gas molecule–molecule interactions are modeled with the cut-and-shifted LJ 6–12 potential with a cut-off distance $r_c = 15.2$ Å ($4.0\sigma_{CH4}$) (Firouzi and Wilcox, 2012; Firouzi et al., 2003, 2004, 2006, 2007; Xu et al., 2000a). To calculate the interactions between the gas molecules and the walls, the LJ potential for the interactions between the gas molecules and the individual carbon atoms on the pore network structure are used with a cut-off distance $r_c = 13.3$ Å ($3.5\sigma_{CH4}$). The interaction between the gas molecules with the entire carbon porous structure was taken to be the sum of the LJ potentials between the gas molecules and each individual carbon atom in the pore network (Firouzi and Wilcox, 2012). The flux, J, in the direction of the applied pressure gradient is calculated by measuring the net number of gas molecules crossing a given yz plane. The permeability, K, is then calculated using:

$$K = \frac{J}{\Delta P/L} = \frac{LJ}{\Delta P}, \tag{6}$$

where ΔP and L are the pressure drop imposed along the pore network and length of the pore network, respectively. To study gas transport due to an applied pressure gradient, the temperature of the system is held constant at 25 °C thereby eliminating any contribution of the temperature gradient to the transport; hence, isokinetic conditions are maintained by rescaling the velocity independently in all three directions.

Table 2
XRD and XPS compositions of Eagle Ford core sample.

XRD composition, %					
Quartz	Feldspar	Calcite	Pyrite	Clay	TOC
22.7	1.2	53.3	4.7	12.3	4.83
XPS composition, %					
O	C	Ca	Si	Al	N
46.93	34.04	4.71	8.33	5.98	0

3. Gas permeability measurements of shales

Measurements of helium permeability are made to compare against the modeling predictions. The history-match method was outlined below to measure the permeability of an Eagle Ford shale sample. The sample is horizontal (parallel to bedding) from a depth of 12,753 ft and has XRD and XPS mineral compositions as indicated in Table 2.

3.1. Pressure pulse decay experiment

The pressure pulse decay experiment is useful to measure gas permeability of cores from tight formations that are in the micro Darcy range or less. The concept of this method relies on placing the core inside a holder that is connected to an upstream volume and a downstream volume. Fig. 1 shows a schematic of the experimental setup. Initially, the pressure exerted is the same everywhere in the system. A closed (main) valve separates the upstream chamber from the core and the downstream volume. The upstream pressure is increased to a value greater than the initial pressure that exists in the core and downstream chamber. After that, the main valve is opened and gas is allowed to flow from the upstream chamber to the core and the downstream chamber. This is the so-called pressure pulse. The pressure history is monitored and recorded using pressure transducers located in the

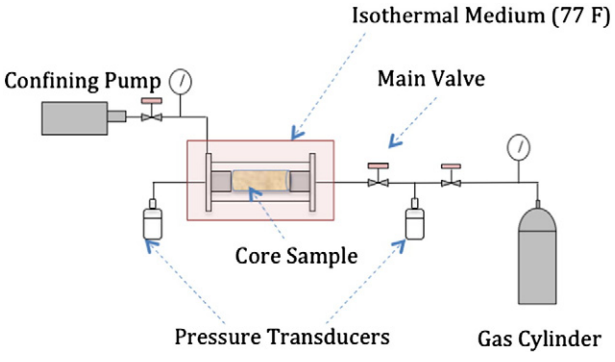

Fig. 1. Schematic of the experimental setup. Upstream pressure is initially higher than the core and downstream pressures. The core and downstream pressures are the same. After opening the main valve, the pressure flows to the core and eventually equilibrate everywhere in the system.

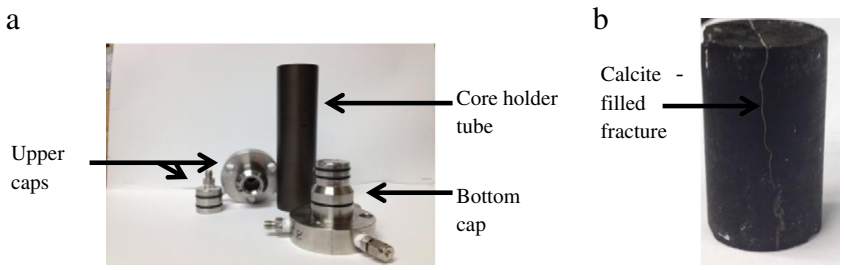

Fig. 2. (a) Core holder apparatus, (b) Core sample. The core holder apparatus consists of bottom cap, core holder and upper cap. The core is placed above the bottom cap. The core holder connects the core and bottom cap with the upper cap. The bottom cap is connected to the upstream volume while the upper cap is connected to the downstream volume.

upstream and downstream chambers. Once the pressure equilibrates in the system, upstream and downstream pressure histories are used for permeability measurements.

The apparatus of the pulse decay experiment consists of three main components: bottom cap, upper cap and stainless steel tube, as shown in Fig. 2a. The core plug used in the permeability study is sampled from the Eagle Ford shale play and has a clear calcite filled fracture along the length of the core as shown in Fig. 2b.

The sample is placed on the bottom cap and a Teflon heat-shrinkable tube is used to wrap the sample. Another layer of the shrinkable tube is spread with a sealant (730 Solvent Resistant Sealant, Dow Corning) from inside and wrapped around the sample as Fig. 3 indicates. The sample, then, is wrapped with aluminum foil and nickel foil to prevent helium gas from diffusing through the sleeve material to the confining volume. This wrapping order is made twice and is allowed three days to dry. After putting together the apparatus, two pressure transducers (Super TJE Model) and a temperature controller (Omega CN8200 Series) are used. The temperature of the sample is kept constant at 77 °F. A water pump is used to apply confining pressure on the sample.

3.2. History-match method

Simplified analytical solutions are commonly used to estimate the permeabilities of tight rock samples (Civan et al., 2012). Typical methods as attributed to Brace et al. (1968), Amaefule et al. (1986), Dicker and Smits (1988) and Jones (1997) may be effectively used for permeability measurements in pressure pulse decay experiments but are subject to significant limitations. Because gas is highly compressible, these solutions generally provide reasonably accurate measurements at a maximum pressure pulse of 10% of the initial pressure. Some solutions account for sorption effects such as those investigated by Jones (1997), while others such as those investigated by Brace et al. (1968) do not. The experimental conditions provided in the current study exceed the 10% pressure drop limitation; therefore, a numerical solution including gas compressibility is employed to estimate the gas permeability via history-matching the pressure drop rather than the Brace method.

The history-match method is based on a numerical flow simulation and is employed to estimate the gas permeability by matching the simulated pressure history with the experimental result. Specifically, the upstream and downstream pressure histories are matched simultaneously. It is very common to apply a 5–10% pressure pulse during pressure pulse decay experiments and use simple analytical solutions to estimate the gas permeability. The history-match method, however, can be used to estimate the gas permeability at large pressure pulses. The advantage of a large pressure pulse is the improved signal to noise ratio of the pressure data.

In this study, a fully implicit 2-D single-phase, compressible-gas simulator was written to study the gas transport characteristics through shale cores and to be used as a means of inferring gas permeability by matching of pressure history. The simulator uses the black oil model and a standard upstream-weighted finite volume approach (Aziz and Settari, 1979). The Newton–Raphson method was used to resolve non-linearity in pressure terms. The gas flux is described by Darcy's law without diffusion as appropriate for the large pressure pulses employed. The gas properties, i.e. viscosity and compressibility, are dynamic and are estimated using NIST data (NIST Webbook, 2013) and the Peng-Robinson equation of state (Peng and Robinson, 1976), respectively. An in-situ 2-D porosity map of the core obtained by a CT-Scanning method as well as examples of pressure pulse history-match is found in Alnoaimi and Kovscek (2013).

The numerical scheme is fully implicit. The gas compressibility makes the transmissibility terms very sensitive to pressure change and therefore explicit schemes cannot be used for this problem. The general equation solved in a discretized form is

$$\frac{\partial}{\partial x}\left(\alpha\frac{A_x k}{\mu_g B_g}\frac{\partial p}{\partial x}\right)\Delta x+\frac{\partial}{\partial y}\left(\alpha\frac{A_y k}{\mu_g B_g}\frac{\partial p}{\partial y}\right)\Delta y=V_b\frac{\partial}{\partial t}\left[\varnothing\frac{1}{B_g}+(1-\varnothing)\rho_m V_g\right], \tag{7}$$

where α is the transmissibility conversion factor, A is the cross-sectional area, k is the measured permeability and is assumed to be equal in the x and y directions, μ_g is the gas viscosity, B_g is the gas formation volume factor, V_b is the block volume, ρ_m is the rock density and V_g is the volume of adsorbed gas. Sorption effects are ignored in this work because helium is considered a non-adsorptive gas.

After measuring the apparent permeability, the liquid permeability and slip factor are estimated using Eq. (3). The average pore diameter

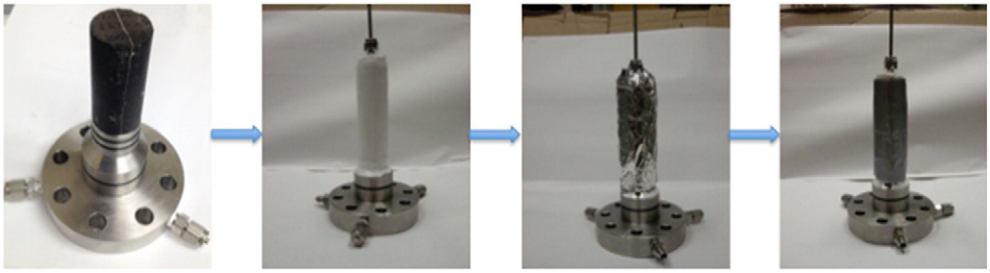

Fig. 3. Wrapping procedure for the core sample. The core is placed on the bottom cap and wrapped with three Teflon heat-shrinkable tubes with white silicon gel spread in between the layers. The sample is additionally wrapped with aluminum and nickel foils to prevent helium escape from the core to the confining volume.

Table 3
Pressure pulse decay experimental conditions.

Experiment	Downstream pressure, psi	Upstream pressure, psi	Final pore pressure, psi	Confining pressure, psi
1	146.00	294.00	227.40	731.58
2	146.00	367.50	270.10	763.00
3	146.00	441.00	312.80	818.00
4	146.00	514.50	347.63	847.63
5	146.00	588.00	386.32	886.32
6	146.00	661.50	425.00	925.00

carrying gas is inferred from the liquid permeability using Eq. (8) as provided in (Civan, 2010)

$$R = \frac{4}{b_a}\mu\sqrt{\frac{\pi R_g T}{2M_w}}, \tag{8}$$

where R is the pore radius, b_a is the slip factor, R_g is the gas constant, T is the temperature and M_w is the gas molecular mass. This equation is used to estimate the apparent pore radius after fitting a straight line to the apparent permeability versus reciprocal pressure plot.

3.3. Experimental conditions

The pressure pulse decay experimental conditions mimic the conditions applied in the MD simulation. The experimental conditions are listed in Table 3. The confining pressure is increased in every experiment to set the net effective stress (i.e., the difference in confining and pore pressure) constant at about 500 psi. Pore pressure, as used here, is the gas pressure within the pore space of the sample. The confining pressure is adjusted every time the pore pressure increases.

In what follows, we present and discuss the results of our simulations and experiments.

4. Results and discussion

NEMD simulations for modeling the transport properties of helium are conducted. To better understand the distributions of helium in the pore, Fig. 4 presents the time-averaged density profiles, $\rho_i^z(x)$(averaged in the yz planes), of helium as a function of x along the pore, defined as the region, $-51.1 < x < 51.1$ Å. Profiles are computed by averaging the results over the last 1,000,000 time steps. To calculate $\rho_i^z(x)$, the simulation box in the x-direction was divided into grids of size 5.1 Å, and for each MD step, the density profiles $\rho_i^z(x)$ were obtained by averaging the number of gas molecules over the distance 5.1 Å. In this and subsequent figures, the vertical dashed lines indicate the boundaries of the pore region. The density profiles are essentially flat in the two CVs, with numerical values that match those obtained by the GCMC method at the same conditions, indicating that the chemical potentials in the two CVs have been properly maintained during the NEMD simulations. As seen in Fig. 4, in the transport region, i.e., $-51.1 < x < 51.1$ Å, the density decreases along the pore, as expected. The density in the transport region is low due to the minimal adsorption that helium exhibits. The density profiles in the transport region are not linear due to the existence of the overall bulk pressure gradient and the diffusive and convective fluxes that make up the total flux. These features are clearly seen in Fig. 5, where we show snapshots of the same pore and the distribution of the gas molecules for the same conditions as in Fig. 4, obtained at a steady state after 10×10^6 time steps. From this figure it is evident that the density decreases from left to right.

Fig. 6 represents the dependence of the permeability of helium on the inverse mean pressure applied to the generated pore network model. The downstream pressure is fixed at 146.96 psi, while the upstream pressures are varied. The gas permeabilities have been converted using the bulk viscosity to convert from generalized permeability units to "micro-Darcy" units (a common unit used in petroleum engineering) and the slippage factor b and k_∞ have been calculated using Eq. (3). By increasing the upstream pressure but maintaining the same downstream pressure along the pore, the permeability of helium decreases. This phenomenon is described by the theory of Klinkenberg in that at the lower pressures the mean free path increases thereby increasing the slippage effect and leading to enhanced gas permeability, while at the larger mean pressures the slippage effect is suppressed leading to reduced permeability. The same behavior for CH_4 and CO_2 gases are found in previous work (Firouzi and Wilcox, 2013).

The apparent permeability values for helium are listed in Table 4. The values are the early-time apparent permeability that represents flow in the largest pore space (i.e., macro-pores). The estimated permeabilities are in the micro-Darcy range and this is found to be common in Eagle Ford samples as observed in our laboratory measurements. Fig. 7 shows a plot of the apparent permeability versus the reciprocal pore pressure with a straight line fit to determine the liquid permeability and slip factor. The error bars in the data found in the figure represent the ±5% uncertainty in the volumetric measurements of the apparatus. The liquid permeability is 39.31 micro-Darcy and the slip factor is 69.91 psi. The slip factor is used to determine an apparent pore diameter from Eq. (8). The estimated apparent pore diameter for a cylindrical pore shape is 324.4 nm. This average pore size is inferred from the net effective stress applied to the sample that eventually dictates the slip factor. The estimated Knudsen number for each experiment falls in the slip-flow regime as mentioned earlier in Table 1.

The average pore size in the 3-D pore network used in the MD simulation is 2 nm, hence the calculated permeability represents flow in micro and mesopores. It is computationally very expensive to carry

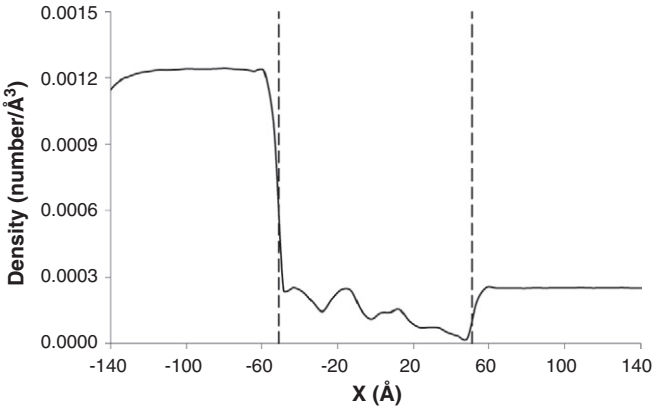

Fig. 4. Time-averaged density $\rho^z(x)$ profile of helium in the transport direction x. The upstream and downstream pressures are 734.80 and 146.96 psi, respectively. Dashed vertical lines indicate the boundaries of the pore network region.

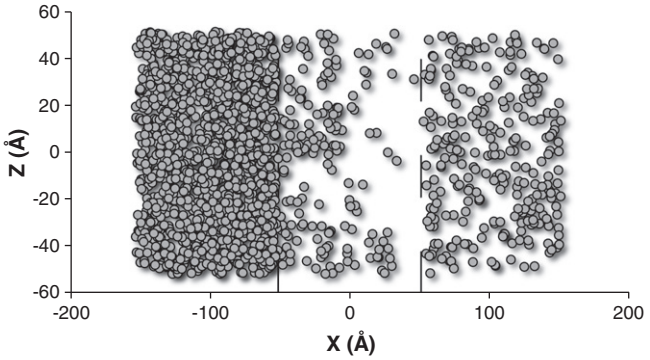

Fig. 5. A snapshot of the distributions of helium in the pore network. The upstream and downstream pressures are 734.80 and 146.96 psi, respectively. Dashed vertical lines indicate the boundaries of the pore network region.

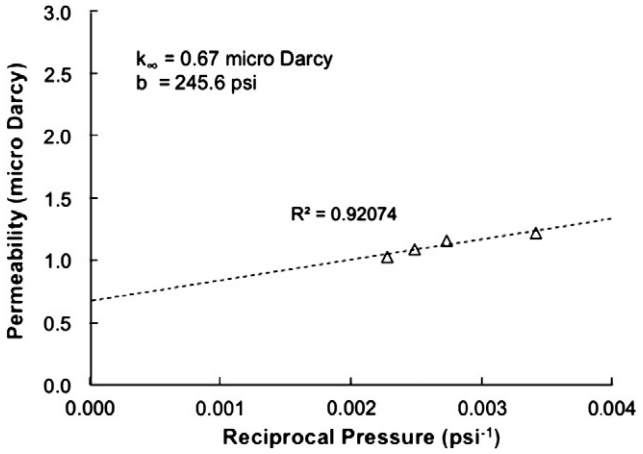

Fig. 6. The dependence of the permeability of helium on inverse mean pressure applied to the pore network. The downstream pressures are fixed at 146.96 (psi) while the upstream pressure varies.

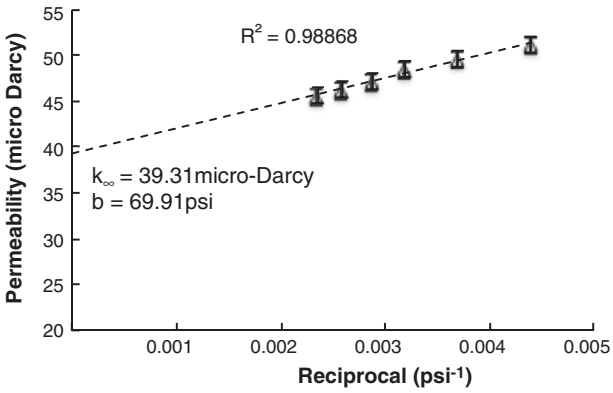

Fig. 7. Apparent permeability versus reciprocal pressure.

out MD simulations within a 3-D pore network with an average pore size comparable to those of realistic natural systems. The gas permeability obtained by the pulse decay experiment is about a magnitude greater than that calculated by the MD simulation. Gas transport is typically enhanced in micro and mesopores due to molecular streaming or Knudsen diffusion over Darcy flow where the gas velocity at the pore walls is non-zero and the "gas slippage" reduces viscous drag and increases permeability (Firouzi and Wilcox, 2013). The experimental permeability measurements of the intact core are greater than those obtained by the MD simulations because the core contains multi-pore sizes including macro- and meso-pores. The experimental permeability is extracted from the early-time pressure profile that corresponds to macropores as indicated by the estimated apparent pore diameter. This permeability is referred to as Darcy permeability. One way to bridge the gap in scale between the two measurements is through crushing the intact core using a grinding tool to very fine powders and using a sieve to control the grain size. In addition, an adsorption isotherm can be obtained for the sample using nitrogen gas to estimate the average pore diameter. Once the estimated average pore diameter is equivalent to 2 nm, the permeability measurements would be comparable to MD simulations. Although such a method would change the nature of the shale sample, it is still insightful to study the adsorption characteristics of gases in shales for the purpose of evaluating shales as a CO_2 storage media.

5. Summary

NEMD simulations are conducted, with an external driving force imposed on a 3-D pore network model representative of carbon-based structure of coal and shale. These simulations investigate the transport properties of helium as a non-adsorptive gas to predict the permeability and Klinkenberg parameters. The 3-D carbon pore network is generated atomistically using the Voronoi tessellation method and simulations are conducted to determine the effect of pressure on gas permeability within the pore network structure.

Table 4
Gas permeability at increasing pore pressure.

Experiment	Permeability, micro-Darcy	Pore pressure, psi	Reciprocal pressure, psi	Knudsen number
1	51.2	227.40	0.0044	2.59×10^{-2}
2	49.6	270.10	0.0037	2.18×10^{-2}
3	48.5	312.80	0.0032	1.88×10^{-2}
4	47.1	347.63	0.0029	1.69×10^{-2}
5	46.3	386.32	0.0026	1.52×10^{-2}
6	45.7	425.00	0.0024	1.38×10^{-2}

Experimental analyses have been conducted using the pressure pulse decay technique with the aid of a numerical solution to history match the pressure history and determine helium permeability and Klinkenberg parameters of a shale core plug at similar conditions. The comparison between conventional laboratory permeability measurements and the predicted permeability using MD simulations indicates that the gas permeability, obtained by the pulse decay experiment, is approximately two orders of magnitude greater than that calculated by the MD simulation. The estimated experimental permeability, however, is extracted from the early-time pressure profile corresponding to transport in macropores as indicated by the estimated apparent pore diameter and referred to as a Darcy permeability. Crushing the intact core and sieving the sample to control the grain size may bridge the gap in scale between the two methods in a way that the permeability measurements may be comparable with the simulations. Coal and the organic components of shale are comprised of an extremely complex pore structure with surface functionality and natural fractures. More complex molecular models of graphite structures containing fractures, local charge and defect sites within the pores, in addition to the inclusion of chemical functional groups inside the cavities to generate a more realistic model of natural systems of interest such as coal and shales, will be considered in the future work. These results will potentially have important implications on gas transport in carbon-based materials and geologic formations and may provide an understanding of the limitations of the use of continuum fluid to model transport properties for confined fluids.

Acknowledgments

Portions of this work were supported by the US DOE under DE-FE-0004731. The views and opinions of the authors expressed herein do not necessarily state or reflect those of the United States Government or any agency thereof. The computations were carried out on the Center for Computational Earth & Environmental Science (CEES) cluster at Stanford University. Also, we would like to thank Dennis Michael for his administration of CEES and assistance in the installation of our simulation codes.

References

Akkutlu, Y., Fathi, E., 2012. Multiscale gas transport in shales with local kerogen heterogenities. SPE J. 17 (4), 1002–1011.

Alnoaimi, K.R., Kovscek, A.R., 2013. Experimental and numerical analysis of gas transport in shale including the role of sorption. Paper SPE 166375, Presented at the SPE Annual Technical Conference and Exhibition Held in New Orleans, Lousiana, USA, 30 September–2 October.

Amaefule, J.O., Wolfe, K., Walls, J.D., Ajufo, A.O., Peterson, E., 1986. Laboratory determination of effective liquid permeability in low-quality reservoir rocks by the pulse decay technique. Paper SPE 15149, Presented at the 56th California Regional Meeting of the Society of Petroleum Engineers Held in Oakland, CA, April 2–4.

Aziz, K., Settari, A., 1979. Petroleum Reservoir Simulation. Blitzprint Ltd., Calgary, Alberta (printed by).
Bitsanis, I., Vanderlick, T., Tirrel, M., Davis, H., 1988. A tractable molecular theory of flow in strongly inhomogeneous fluids. J. Chem. Phys. 89 (5), 3152.
Brace, W.F., Walsh, J.B., Frangos, W.T., 1968. Permeability of granite under high pressure. Journal of Geophysical Research 73 (6) (March 15).
Bravo, M., 2007. Effects of transition from slip to free molecular flow on gas transport in porous media. J. Appl. Phys. 102 (7), 074905.
Chawathe, A., Ertekin, T., Grader, A., 1996. Understanding multimechanistic gas–water flow in fractured reservoirs: mapping of the multimechanistic flow domain. Paper SPE 36738, Presented at the SPE Annual Technical Conference and Exhibition Held in Denver, Colorado, 6–9 October.
Civan, F., 2010. Effective correlation of apparent gas permeability in tight porous media. Transp. Porous Media 82 (2), 375–384.
Civan, F., Rai, C.S., Sondergeld, C.H., 2012. Determining shale permeability to gas by simultaneous analysis of various pressure tests. SPE J. 17 (3), 717–726 (144253).
Cracknell, R., Nicholson, D., Quirke, N., 1995. Direct molecular-dynamics simulation of flow down a chemical-potential gradient in a slit-shaped micropore. Phys. Rev. Lett. 74, 2463–2466.
Curtis, M.E., Amborse, R.J., Sondergeld, C.H., Rai, C.S., 2011. Transmission and scanning electron microscopy investigation of pore connectivity of gas shales on the nanoscale. Paper SPE 144391, Presented at the North American Unconventional Gas Conference and Exhibition Held in Woodlands, Texas 14–16 June.
Dicker, A.I., Smits, R.M., 1988. A practical approach for determining permeability from laboratory pressure-pulse decay measurements. Paper SPE 17578, Presented at the SPE International Meeting on Petroleum Engineering, Held in Tianjin, China, November 1–4.
Ertekin, T., King, G.R., Schwerer, F.C., 1986. Dynamic gas slippage: a unique dual-mechanism approach to the flow of gas in tight formations. SPE J. Form. Eval. 1 (1), 43–52.
Firouzi, M., Wilcox, J., 2012. Molecular modeling of carbon dioxide transport and storage in porous carbon-based materials. Microporous Mesoporous Mater. 158, 195–203.
Firouzi, M., Wilcox, J., 2013. Slippage and viscosity predictions in carbon micropores and their influence on CO_2 and CH_4 transport. J. Chem. Phys. 138, 064705.
Firouzi, M., Tsotsis, T., Sahimi, M., 2003. Nonequilibrium molecular dynamics simulation of transport and separation of supercritical fluid mixtures in nanoporous membranes. I. Results for a single carbon nanopore. J. Chem. Phys. 119 (13), 6810.
Firouzi, M., Nezhad, M., Tsotsis, T., Sahimi, M., 2004. Molecular dynamics simulations of transport and separation of carbon dioxide–alkane mixtures in carbon nanopores. J. Chem. Phys. 120 (17), 8172.
Firouzi, M., Sahimi, M., Tsotsis, T., 2006. Supercritical fluids in porous composite materials: direction-dependent flow properties. Phys. Rev. E. 73, 036312.
Firouzi, M., Tsotsis, T., Sahimi, M., 2007. Molecular dynamics simulations of transport and separation of supercritical carbon dioxide–alkane mixtures in supported membranes. Chem. Eng. Sci. 62 (10), 2777–2789.
Ford, D.M., Glandt, E.D., 1995. Molecular simulation study of the surface barrier effect: dilute gas limit. J. Phys. Chem. 99 (29), 11543–11549.
Ford, D.M., Heffelfinger, G.S., 1998. Massively parallel dual control volume grand canonical molecular dynamics with LADERA II. Gradient driven diffusion through polymers. Mol. Phys. 94 (4), 673–683.
Furukawa, S., Hayashi, K., Nitta, T., 1997. Effects of surface heterogeneity on gas permeation through slit-like carbon membranes by non-equilibrium molecular dynamics simulations. J. Chem. Eng. Jpn 30, 1107–1112.
Gamson, P., Beamish, B., Johnson, D., 1993. Coal microstructure and micro-permeability and their effects on natural gas recovery. Fuel 72, 87–99.
Hadjiconstantinou, N.G., 2006. The limits of Navier–Stokes theory and kinetic extensions for describing small-scale gaseous hydrodynamics. Phys. Fluids 18, 111301–111319.
Heffelfinger, G., Ford, D., 1998. Massively parallel dual control volume grand canonical molecular dynamics with LADERA I. Gradient driven diffusion in Lennard-Jones fluids. Mol. Phys. 94 (4), 659–671.
Heffelfinger, G., Swol, F., 1994. Diffusion in Lennard-Jones fluids using dual control volume grand canonical molecular dynamics simulation (DCV-GCMD). J. Chem. Phys. 100 (10), 7548.
Jalali, J., Mohaghegh, S., 2004. A Coalbed Methane Reservoir Simulator Designed and Developed for the Independent Producers. Paper SPE 91414, Presented at the SPE Eastern Regional Meeting Held in Charleston, West Virginia, 15–17 September.
Javadpour, F., Fisher, D., 2007. Nanoscale gas flow in shale gas sediments. J. Can. Petrol. Technol. 46 (10).
Johnson, J., Zollweg, J., Gubbins, K., 1993. The Lennard-Jones equation of state revisited. Mol. Phys. 78 (3), 591–618.
Jones, S.C., 1997. A technique for faster pulse-decay permeability measurements in tight rocks. Paper SPE 28450, Presented at the SPE Annual Technical Conference and Exhibition Held in New Orleans, 25–28 September.
Jones, F., Owens, W., 1980. A laboratory study of low permeability gas sands. J. Pet. Technol. 32, 1631–1640.
Kjelstrup, S., Hafskjold, B., 1996. Nonequilibrium molecular dynamics simulations of steady-state heat and mass transport in distillation. Ind. Eng. Chem. Res. 35, 4203–4213.
Klinkenberg, L.J., 1941. The permeability of porous media to liquid and gases. API Drill. Prod. Pract. 41, 200–213.
Lupkowski, M., Swol, F., 1991. Ultrathin films under shear. J. Chem. Phys. 95 (3), 1995.
MacElroy, J., 1994. Nonequilibrium molecular dynamics simulation of diffusion and flow in thin microporous membranes. J. Chem. Phys. 101 (6), 5274.
Maginn, E., Bell, A., Theodorou, D., 1993. Transport diffusivity of methane in silicalite from equilibrium and nonequilibrium simulations. J. Phys. Chem. 97 (16), 4173–4181.
McPhee, C.A., Arthur, K.G., 1991. Klinkenberg permeability measurements: problems and practical solutions. In: Worthington, P.F. (Ed.), Advances in Core Evaluation: Accuracy and Precision in Reserves Estimation, pp. 447–462.
Mulder, M., 1991. Basic Principles of Membrane Technology. Kluwer Academic Publishers, Dordrecht.
Naserifar, S., Liu, L., Goddard, W.A., Tsotsis, T.T., Sahimi, M., 2013a. Toward a Process-based molecular model of SiC membranes. 1. Development of a reactive force field. J. Phys. Chem. C 117, 3308–3319.
Naserifar, S., Goddard, W.A., Liu, L., Tsotsis, T.T., Sahimi, M., 2013b. Toward a process-based molecular model of SiC membranes. 2. Reactive dynamics simulation of the pyrolysis of polymer precursor to form amorphous SiC. J. Phys. Chem. C 117, 3320–3329.
Neuman, S., 1977. Theoretical derivation of Darcy's law. Acta Mech. 25, 153–170.
Nicholson, D., Cracknell, R., Quirke, N., 1996. A transition in the diffusivity of adsorbed fluids through micropores. Langmuir 12 (16), 4050–4052.
NIST, 2013. National Institute of Standards and Technology. http://webbook.nist.gov/chemistry/fluid/.
Peng, D., Robinson, D., 1976. A new two-constant equation of state. Ind. Eng. Chem. Fundam. 15 (1), 59–64.
Pohl, P., Heffelfinger, G., 1999. Massively parallel molecular dynamics simulation of gas permeation across porous silica membranes. J. Membr. Sci. 155 (1).
Sahimi, M., Tsotsis, T., 2003. Molecular pore network models of nanoporous materials. Physica B 338, 291–297.
Sondergeld, C.H., Ambrose, R.J., Rai, C.S., Moncrieff, J., 2010. Micro-structural studies of gas shales. Paper SPE 131771, Presented at the SPE Unconventional Gas Conference Held in Pittsburgh, Pennsylvania, USA, 23–25 February.
Sun, M., Ebner, C., 1992. Molecular-dynamics simulation of compressible fluid flow in two-dimensional channels. Phys. Rev. A 46 (8), 4813–4818.
Sunderrajan, S., Hall, C., Freeman, B., 1996. Estimation of mutual diffusion coefficients in polymer/penetrant systems using nonequilibrium molecular dynamics simulations. J. Chem. Phys. 105 (4), 1621.
Thompson, A., Ford, D., Heffelfinger, G., 1998. Direct molecular simulation of gradient-driven diffusion. J. Chem. Phys. 109 (15), 6406.
Travis, K., Todd, B., Evans, D., 1997. Departure from Navier–Stokes hydrodynamics in confined liquids. J. Phys. Rev. 55 (4), 4288–4295.
Vega, B., Dutta, A., Kovscek, A.R., 2013. CT imaging of low permeability, dual-porosity systems using high x-ray contrast gas. Transp. Porous Media (submitted for publication).
Vijaya, M., Ramana, I., Madan, K., Ravi, C., 2012. Microstructure study of high performance concrete containing supplementary cementing materials. Int. J. Adv. Sci. Tech. Res. 5 (2), 435–444.
Whitaker, S., 1986. Flow in porous media I: a theoretical derivation of Darcy's Law. Transp. Porous Media 1, 3–25.
Xu, L., Sedigh, M., Sahimi, M., Tsotsis, T., 1998. Nonequilibrium molecular dynamics simulation of transport of gas mixtures in nanopores. Phys. Rev. Lett. 80 (16), 3511–3514.
Xu, L., Tsotsis, T., Sahimi, M., 1999. Nonequilibrium molecular dynamics simulation of transport and separation of gases in carbon nanopores. I. Basic results. J. Chem. Phys. 111 (7), 3252.
Xu, L., Sahimi, M., Tsotsis, T., 2000a. Nonequilibrium molecular dynamics simulations of transport and separation of gas mixtures in nanoporous materials. Phys. Rev. E. 62, 6942.
Xu, L., Sedigh, M., Tsotsis, T., Sahimi, M., 2000b. Nonequilibrium molecular dynamics simulation of transport and separation of gases in carbon nanopores. II. Binary and ternary mixtures and comparison with the experimental data. J. Chem. Phys. 112 (2), 910.
Yoshioka, A., Yasumoto, A., Kishi, K., Tsuru, T., 2008. MD simulation studies for effect of membrane structures and dynamics on gas permeation properties through microporous amorphous silica membranes. Desalination 233, 333–341.